Interplay of electronic structure and magnetism in Fe₂- and Rh₂-based Heusler alloys

Danil R. Baigutlin [1] Vladimir V. Sokolovskiy [1,2] and Vasiliy D. Buchelnikov [1]

[1]*Faculty of Physics, Chelyabinsk State University, 454001 Chelyabinsk, Russia*
[2]*National University of Science and Technology "MISiS," Moscow 119049, Russia*

In this work, we present a comparative study of the structural, elastic, electronic, magnetic, and transport properties of Heusler alloys Fe₂RhZ and Rh₂FeZ with Z = Al, Si, Ga, Ge, In, Sn using the density functional theory. The strongly constrained and appropriately normed functional is considered for the exchange-correlation functional. The newly Heusler T-type pseudocubic structures, T^p and T^c, with alternating layers and columns of Fe and Rh along the [001] direction being ≈26 meV/atom lower in energy than the inverse XA structure are predicted as ground states for the Fe₂RhZ family. According to the convex hull analysis, all the considered alloys are thermodynamically and mechanically stable or meta-stable. Hybridization schemes and their role in the formation of half-metallicity depending on the weak tetragonal distortion are discussed. XA-Fe₂RhSi is only predicted to be half-metallic in the minority channel with 100% spin polarization and integer magnetic moment of $5\mu_B$, while the ground state T structure with layered ordering of Fe and Rh is characterized by the 73% polarization due to a pseudogap around Fermi level. Additionally, a large Seebeck coefficient and figure of merit for the spin-down channel of XA-Fe₂RhSi is predicted.

I. INTRODUCTION

Density functional theory (DFT) calculations have an important role in the study of the ground state properties of materials aimed to predict new functional properties, materials, or phases that are difficult to observe experimentally. Intermetallic alloys have always been an important test system for various DFT approximations. Difficulties in their description are related to the presence of strongly localized electrons, which makes it difficult to accurately predict their equilibrium properties and especially the band gap width at Fermi energy E_F. As is well known, the half-local generalized gradient approximation (GGA) functionals fail to predict the ground state half-metallic (HM) properties. However, this problem can be usually solved by introducing the Hubbard parameter U [1–3].

On the other hand, the modern meta-GGA schemes which properly balance the nonlocality contributions to the exchange and correlation, are meant to solve the band gap problem for the strongly correlated d-electron intermetallics [4–8]. In this regard, the HM Heusler alloys exhibiting the absence of the density of electronic states (DOS) for one spin channel at E_F are excellent study objects in terms of exchange-correlation effects.

Among HM Heusler alloys, the wide variety of compounds based on the $3d$ transition metals (Co, Mn, Ti, V, Cr, Fe, Ni) attracted sustained attention from both an experimental and a theoretical point of view due to their HM band structure and magnetic properties, which make them suitable for technical applications (see, e.g., Refs. [9–13], and references therein).

On the contrary, there is much less information about HM Heusler alloys consisting of $4d$ elements. The investigation of $4d$ Heusler alloys is interesting in view of the fact that the lattice thermal conductivity as well as the mobility of atoms can be reduced when light $3d$ elements are replaced by heavier $4d$ elements. As a consequence, one can expect an increase in the efficiency of thermal current generation and transport properties [14]. Over the past decade, the interest of researchers has turned to Zr₂- [15–19], Y₂- [20], Ru₂- [21–24], and Rh₂- [25] based Heusler compounds with $3d$ transition elements exhibiting half-metallicity.

The *ab initio* research of the Zr₂YZ family (Y = V, Cr, Co, Ni; Z = B, Al, Ga, In, Si, Ge, Sn, Pb) with the regular $L2_1$ and inverse XA structures aimed to investigate their ground state properties may be found in Refs. [15–18]. For all alloys, XA is reported to be preferable except Zr₂VZ. It was shown that the electronic structure of XA and $L2_1$ reveals the HM and metallic character, respectively. Khelfaoui *et al.* reported that Zr₂PdZ (Z = Al, Ga, In) possess the $L2_1$ ground state structure despite its mechanical instability followed from the negative shear modulus as compared to the HM XA structure [26].

Recently, Birsan and Kuncser revealed that the HM character in Zr₂CrAl is preserved during phase transitions between the cubic XA structure and the tetragonal, orthorhombic, and rhombohedral structures [19]. This finding is a consequence of the fact that the ferrimagnetic exchange coupling between Zr and Cr atoms does not depend on symmetry reduction. Kang and Zhang focused on the origin of the gap in Y₂CrZ (Z = Al, Ga, In) with the ferromagnetic (FM) ground state XA structure exhibiting perfect half-metallicity [20]. The origin of the gap is due to d-d orbital hybridization between the Y and Cr atoms similarly to the mechanism for $3d$ HM Heusler alloys [27]. The gap is stable over a wide range of pressures.

The *ab initio* studies of Ru₂-based heavy alloys may be found in Refs. [21–24]. In contrast to Y₂- or Zr₂-based compounds with XA structure, Ru₂-based alloys have the preferred $L2_1$ structure. The mechanical stability of the

$L2_1$ phase is provided by the calculations of the elastic moduli [21,22]. Notice that Ru_2-based alloys are mostly ductile, which makes them preferable for practical applications. A detailed analysis of the Poisson and Pugh ratios confirms the ductility of Ru_2CrGa and $Ru_2Fe(Ge, Si, Sn)$ and the brittleness of Ru_2MnGa and Ru_2CoGa [21,22].

An origin of the HM electronic properties of X_2YZ Heusler alloys containing $4d$ elements have been systematically studied by Ghosh and Ghosh [28] for 54 compounds with $X =$ Mn, Fe, Co; $Y =$ Y, Zr, Nb, Mo, Tc, Ru, Rh, Pd, Ag; and $Z =$ Al, Si. They concluded that the hybridization mechanism, which is typical for Heusler alloys with $3d$ elements for X and Y [27], is also valid for $3d$-$4d$ compounds. Venkateswara *et al.* recently reported about experimental and *ab initio* studies of Fe_2RhZ ($Z =$ Ge, Si) [29]. Both alloys crystallize in the XA structure but with disorder in tetrahedral sites between Fe and Rh and reveal the highest Curie temperature (≈ 910 K for $Z =$ Ge and ≈ 940 K for $Z =$ Si) of any known heavy $4d$ or $5d$ Heusler alloys. GGA $+ U$ calculations predict a pure metallic and HM behavior for Fe_2RhGe and Fe_2RhSi, respectively. The HM structure remains stable against the antisite disorder up to 50%. El Amine Monir *et al.* showed that $L2_1$-$Rh_2Fe(Ga, In)$ exhibit HM properties retained over a wide pressure range [25].

It is worth noting that for Fe_2-based Heusler alloys, the newly T^p, T^c, and $T^\#$ structures based on the XA structure are recently found theoretically to be preferable as compared to the XA one [30,31]. The prediction of the newly Heusler-type structures for Fe_2-based alloys suggests that the T structures may also be preferable for other Heusler alloys with the XA structure.

In the context of the present study we wish to emphasize that the understanding of the formation mechanism of the energy gap as well as the prediction of ground state T structures in heavy Heusler alloys are important issues that require a detailed analysis within meta-GGA. We focused attention on the *ab initio* study of the ground state properties of Fe_2RhZ and Rh_2FeZ with different atomic arrangement. The outline of the paper is as follows. Section II contains the details of calculations. Section III is devoted to the discussion of the results of structural properties (Sec. III A), mechanical and thermodynamic stabilities (Sec. III B), electronic and magnetic properties (Secs. III C and III D), and transport properties (Sec. III E). The concluding remarks are given in Sec. IV.

II. COMPUTATIONAL DETAILS

Calculations were performed in the framework of the DFT scheme using the projector augmented-wave method as implemented in the Vienna *Ab initio* Simulation Package (VASP) [32]. The strongly constrained and appropriately normed (SCAN) [33] meta-GGA generation functional was used to approximate the exchange-correlation functional due to several reasons [34]. The plane wave cut-off energy was equal to 460 eV. To generate automatically the k points in the reciprocal space, the gamma-centered scheme was applied. The grid density of ≈ 4000 k points per reciprocal atom was considered for the geometry optimization procedure and with k-mesh density of $\approx 10\,000$ for calculation

of electronic properties. The criteria for total energy convergence and residual atomic forces were set to 10^{-7} and 10^{-2} eV/Å, respectively. The $L2_1$ (space group $Fm\bar{3}m$) and XA (space group $F\bar{4}3m$) Heusler structures as well as T^c, T^p, and $T^\#$ structures [31] based on the XA structure with FM order [35] were chosen for stoichiometric Fe_2RhZ and Rh_2FeZ [see Fig. S1 and Table SI in the Supplemental Material (SM) [36]].

Spin polarization was calculated from

$$P = \frac{DOS_\uparrow^F - DOS_\downarrow^F}{DOS_\uparrow^F + DOS_\downarrow^F} \times 100\%, \quad (1)$$

where subscripts $\uparrow$ and $\downarrow$ mean spin-up and spin-down DOS, and superscript F denotes that the DOSs are considered at the Fermi level.

To perform calculations of the magnetic exchange constants J_{ij}, the Green's function method with the local rigid spin rotation treated as a perturbation [37] and realized in the TB2J python package [38] was implemented. To do this, the maximally localized Wannier functions [39] were firstly calculated by the WANNIER90 code [40]. Further, the set of J_{ij} as a function of the distance between interacting atoms was used as input parameters for the Monte Carlo (MC) simulations of the Heisenberg model with the VAMPIRE 5.0 code [41]. The computational cell contained $\approx 3 \times 10^5$ atoms, and the number of MC steps taken was 10^5.

The basis of Wannier functions was also used to calculate the thermoelectric properties using Boltzmann transport theory using the BOLTZWANN code [42]. The constant relaxation time was equal to $\tau = 10^{-14}$ s. Note that the BOLTZWANN code determines only the electronic part of thermal conductivity and hence the lattice part of thermal conductivity was evaluated by the Slack's equation [43]

$$\kappa_L(\Theta_D, \gamma) = \frac{0.849 \times 5.720 \times 10^7}{2(1 - 0.514\gamma^{-1} + 0.228\gamma^{-2})} \frac{M\Theta_D V^{1/3}}{\gamma^2 n^{2/3} T}, \quad (2)$$

where n is the number of atoms in the primitive unit cell (in the case of full-Heusler alloys $n = 4$), V is the volume of unit cell, M is the molar mass, γ is the Gruneisen parameter, Θ_D is the Debye temperature, and T is the temperature.

III. RESULTS AND DISCUSSION

A. Ground state properties

The results of the geometry optimization (total energy and tetragonal ratio c/a) of the five considered structures of Fe_2RhZ and Rh_2FeZ are shown in Fig. 1. The all values of the total energy are listed in Tables SIV and SV of the SM [36]. It should also be noted that since the tetragonal distortion of the $L2_1$, XA, and T^c structures results in an appearance of two local and global energy minima at $c/a < 1$ and $c/a > 1$, in Fig. 1, we illustrate the results for both minima labeled 1 and 2. It can be seen that for both families of alloys, the simple rule of favorable XA structure with respect to $L2_1$ of X_2YZ alloys is satisfied when the atomic number of the element X is less than the atomic number of the element Y [10]. Namely, the inverse XA structure is preferable for Fe_2RhZ and not preferable for Rh_2FeZ as compared to the regular $L2_1$ or $L1_0$ structures. This finding agrees well with
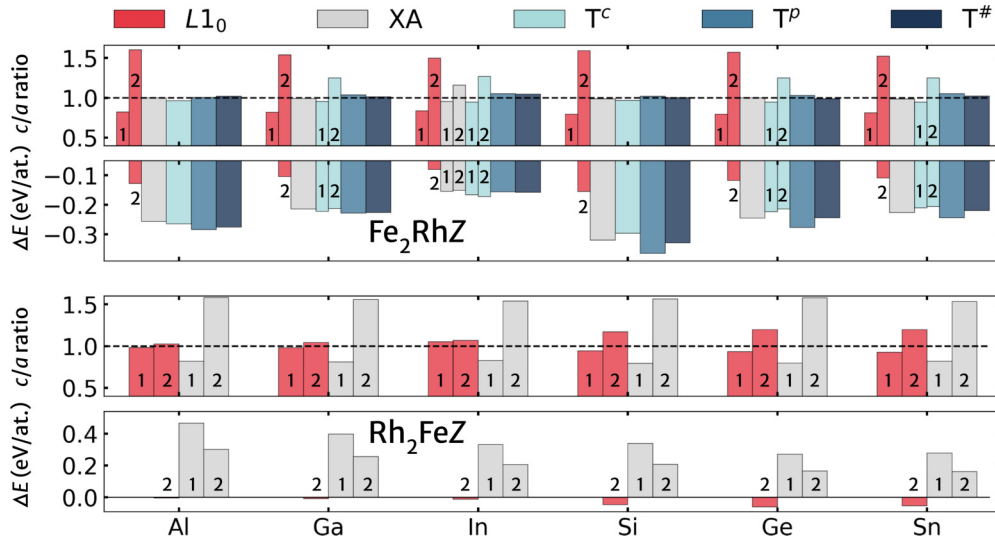
FIG. 1. The total energy difference (ΔE) and tetragonal distortion ratio (c/a) for the ferromagnetically ordered $L1_0$, XA, T^p, T^c, and $T^\#$ structures of Fe_2RhZ and Rh_2FeZ (Z = Al, Si, Ga, Ge, In, Sn). The ΔE is plotted with respect to the energy of the tetragonal distorted $L1_0$ structure with c/a ratio < 1. Labels 1 and 2 denote the energy minima at c/a < 1 and c/a > 1, respectively.

previously reported results [28,45]. However, the proposed T structures based on the XA structure of Fe_2-based alloys turn out to be predominant being in ≈ 26 meV/atom lower in energy compared to the XA structure. In addition, we find that the layered arrangement of Fe and Rh atoms in the T^p structure yields the lowest total energy for all Fe_2-based alloys except Fe_2RhIn with the ground state T^c structure. In addition, the $T^\#$ structure is also found to be preferable with respect to the XA one. We find that both the T^p and $T^\#$ structures are pseudocubic with a small tetragonal distortion, while the T^c structure is calculated to be a tetragonal one with two local and global energy minima at $c/a \neq 1$. The small c/a ratios of the T^p and $T^\#$ structures can be explained by the nonequivalent local atomic arrangement, which gives a chemical pressure, and the absence of the Jahn-Teller splitting in DOS, which is typical for Heusler alloys [11,47]. Here the chemical pressure is a lattice internal force caused by lattice strain with chemical modifications or change in atomic arrangements.

In the case of Rh_2FeZ, the data for T structures are omitted from Fig. 1 because of their significant energy unsuitability compared to the ground state regular Heusler structures. As can be seen, the tetragonal $L1_0$ structure (pseudocubic $L2_1$ phase) with a small c/a ratio is predicted for Rh_2FeAl and Rh_2FeGa, whereas a slightly larger c/a ratio of ≈ 1.06 is found for Rh_2FeIn. An increase in the valence electrons of the Z element leads to an appearance of stable tetragonal $L1_0$ phase with c/a of ≈ 1.19 for a set of Rh_2FeZ with Z = (Si, Ge, In). This suggests the presence of the Jahn-Teller distortion.

The optimized lattice constants and total magnetic moment (μ_{tot}) are given in Table I. For Fe_2RhSi and Fe_2RhGe with XA structure, the calculated values of a and μ_{tot} agree well with the experimental ones [29], whereas, in a case of ground state T^p structure, the estimated lattice constants are found to be 1.4% and 1.9% smaller, correspondingly. The experimental results [29] indicate that both Fe_2RhSi and Fe_2RhGe crystallize in an inverse Heusler structure but with 50% disorder in

tetrahedral sites between Fe and Rh. It means that the close competition in energy between the T^p, $T^\#$, and XA structures (Fig. 1) may hamper the chemical ordering of the samples under typical experimental conditions and makes the inverse XA structure with 50% disorder between tetrahedral site atoms Fe and Rh a likely outcome, rather than the ordered inverse Heusler structure. In addition, the calculated μ_{tot} values are also found to be in good agreement with the experimental ones. It can be seen that Fe_2RhSi is distinguished by its integer magnetic moment obtained theoretically and experimentally [29], which is in good agreement with the Slater-Pauling (SP) rule, and, apparently, Fe_2RhSi should be the HM ferromagnet among all compounds considered in this study.

We would also like to emphasize that for Fe_2RhGe, the GGA-PBE calculations predict the half-metallicity and an integer value of μ_{tot} [45]. However, our calculations within the SCAN functional give the noninteger value of μ_{tot} and the absence of the band gap at E_F (see Table SI and Fig. S5 in the SM [36]), which agrees well with experiment performed by Venkateswara *et al.* [29]. Moreover, the authors have declared the absence of HM behavior in Fe_2RhGe.

For Rh_2FeZ (Z = Al, Ga, In), the optimized lattice constants are calculated to be smaller than the other theoretical [25,46] and experimental [44] values. The discrepancies with the theoretical works [25,46] are caused by a difference in the relaxation procedure and the choice exchange-correlation functional. According to Refs. [25,46], the GGA scheme of the electron relaxation procedure was implemented for a fixed volume of a cubic cell, while in this work both the cell volume and the cell shape were degrees of freedom within the meta-GGA SCAN scheme, which resulted in a tetragonally distorted $L1_0$ structure. Moreover, it is well known that the SCAN predicts a lower optimized volume cell compared to the GGA for the metallic systems [6]. The relative discrepancy in volume cells between ours and published results is about $\approx 4\%$ for In and $\approx 3\%$ for Ga. The discrepancy with the experimental data can be explained by a small deviation from

TABLE I. Calculated lattice constant a (in Å), c/a ratio, and total magnetic moment μ_{tot} (in μ_B/f.u.) for the XA and T^p structures of Fe$_2$RhZ and for the $L1_0$ structure of Rh$_2$FeZ ($c/a > 1.0$). Literature calculated and experimental values are also given; the experimental ones are marked with an asterisk. The type of atomic order is indicated in parentheses.

| | Fe$_2$RhZ | | | | | | Rh$_2$FeZ | | |
| | XA structure | | | T^p structure | | | $L1_0$ structure | | |
Z element	a	c/a	μ_{tot}	a	c/a	μ_{tot}	a	c/a	μ_{tot}
Al	5.836	0.998	5.23	5.814	1.007	5.28	5.892	1.026	4.50
							5.972* (B2) [44]		
Ga	5.878	0.991	5.50	5.775	1.038	5.41	5.881	1.041	4.44
	5.911 [45]	1.000 [45]	5.04 [45]				6.041 [25]		
							6.047 [46]		
							5.978* [44]		
							6.039 [45]	1.000 [45]	4.27 [45]
In	6.205	0.955	5.90	5.990	1.051	5.70	6.044	1.068	4.45
	6.166 [45]	1.000 [45]	5.34 [45]		6.245 [25]				
							6.268 [46]		
							6.251 [45]	1.000 [45]	4.24 [45]
Si	5.768	0.987	5.00	5.687	1.020	5.02	5.579	1.171	4.07
	5.77* [29]		4.98* [29]						
Ge	5.848	0.998	5.23	5.766	1.031	5.12	5.618	1.198	4.10
	5.88* [29]		5.22* [29]				5.671 [45]	0.850 [45]	3.83 [45]
	5.911 [45]	1.000 [45]	4.98 [45]						
Sn	6.122	0.986	5.55	5.980	1.050	5.35	5.817	1.197	4.11
	6.152 [45]	1.000 [45]	5.15 [45]				4.158* (tI8) [44]	0.61* [44]	
							5.883 [45]	0.850 [45]	3.89 [45]

stoichiometry in the experimental samples and the presence of B2 order.

B. Thermodynamic and mechanical stability

To investigate the degree of thermodynamic stability (or instability) of a given phase for all compounds under study, we further performed the convex hull analysis of a set of energy points in the phase space. To accomplish this, we compared the energy of ternary compounds to that of the stable decomposition products and determined the lowest-energy structure of a given phase. The initial geometry of crystal structures for a set of possible stable and unstable compounds composed of Rh, Fe, and Z atoms was taken from the Material Project database [48]. The convex hull diagrams are given in the SM [36] (see Fig. S3). It has been established that Fe$_2$RhZ ($Z =$ Si, Ge) and Rh$_2$FeZ ($Z =$ Al, Ga, Ge, Sn) compounds in their ground state lie on the convex hull, which indicates their chemical stability to decomposition into consistent components. The other alloys are metastable, but the percentage of stable reactions against the decomposition is over 80%. The algorithm for determining the phase stability against decomposition and examples of the calculated decomposition energy E_{dec} are given in the SM [36] (see Sec. II A and Table SVI). The percent of stable reactions against the decomposition is summarized in Table SVII of the SM [36].

Mechanical stability is a further desirable characteristic that supports any crystal's stability and longevity. Elastic behavior can be used to describe a material's capacity to regain its original shape following the absence of a deforming force. The elasticity tensor, which is produced by carrying out finite

lattice distortions and energy-strain relationships, is used to calculate the mechanical properties. The certain elastic properties of Fe$_2$RhZ and Rh$_2$FeZ such as the Poisson's ratio (ν), the Young's modulus (E), and the anisotropy index (A) are given in Table II, and the complete set of independent elastic constants and details of the calculation of the elastic constants are given in the SM [36] (see Sec. II B). It is seen that the ν coefficient for all investigated alloys is greater than 0.27, which indicates the plasticity of the materials and supposedly the predominance of ionic bonds in them [49]. The Young's modulus characterizes the stiffness of a material. When we turn from the XA lattice to the T^p one for Fe$_2$RhZ, an increase in fracture resistance is observed. At the same time, Fe$_2$RhZ and Rh$_2$FeZ have quite similar Young's moduli for the preferred crystal structures, which differ on average by 15%. Another important elastic constant is the anisotropy index A, which shows the unequal mechanical properties in different applications [50]. We mention in passing that when the A values are quite close to 1, the formation of microcracks will be unlikely during the growth of single crystal. It is seen that the sufficiently higher anisotropy values are obvious for the most Fe$_2$RhZ compounds with the XA structure, whereas for T^p-Fe$_2$RhZ and $L1_0$-Rh$_2$FeZ, the A is found to be several times smaller. For Rh$_2$FeGa, we find a good agreement between our calculated values and the values from a previous theoretical study [46]. Our calculations reveal that the XA-Fe$_2$RhAl, T^p-Fe$_2$Rh(Si, Ge), and $L1_0$-Rh$_2$Fe(In, Ge) have the A index close to 1; the difference is in the range from 5% to 20%. This finding allows one to conclude that these single crystals can be synthesized easier compared to the remaining compounds.

TABLE II. Poisson's ratio, Young's modulus E (in GPa), universal anisotropy index A, and Debye temperature Θ_D (in K) for the XA and T^p structures of Fe_2RhZ and for the $L1_0$ structure of Rh_2FeZ ($c/a > 1.0$). Literature calculated values for Rh_2FeGa are also given.

| | Fe₂RhZ | | | | | | | | Rh₂FeZ | | | |
| | XA structure | | | | T^p structure | | | | $L1_0$ structure | | | |
Z	ν	E	A	Θ_D	ν	E	A	Θ_D	ν	E	A	Θ_D
Al	0.316	232.8	1.17	578	0.275	263.3	0.642	705	0.294	277.9	0.276	644
Ga	0.367	164.0	8.23	485	0.327	203.6	2.976	563	0.335	219.6	1.536	531
									0.323 [46]	221.6 [46]	1.929 [46]	
In	0.384	121.1	10.33	372	0.364	134.7	7.646	414	0.323	214.2	0.802	479
Si	0.386	161.7	2.74	549	0.301	275.7	1.053	738	0.342	243.8	1.309	592
Ge	0.341	197.0	2.35	537	0.313	225.2	0.918	611	0.346	217.9	1.198	516
Sn	0.350	170.2	3.67	445	0.327	184.9	1.298	490	0.312	239.3	0.261	505

To discuss a thermodynamic aspect of the T^p phase stability with respect to the inverse XA structure at finite temperatures, we evaluated the free energy F of the structures in a similar fashion as in [31,51], taking into account the vibrational contributions derived within the quasiharmonic Debye model, the electronic contributions from the DOS in terms of the Sommerfeld expansion, and the magnetic contributions obtained within the Heisenberg Hamiltonian, *ab initio* exchange couplings, and MC simulations. The details of the free-energy calculations as well as all temperature-dependent contributions are given in the SM [36] (see Sec. II C and Fig. S4). In Fig. 2, we present the difference in the free energies $\Delta F(T) = F_{T^p}(T) - F_{XA}(T)$ for the $Fe_2Rh(Si, Ge, Sn)$ compounds as a function of temperature T. For all compounds, the T^p structure possesses the lowest free energy already at $T = 0$ K and improves its stability further in the finite-temperature range. It can be seen that the transition between the T^p and XA structures is predicted at about 175, 540, and 700 K for Fe_2RhSi, Fe_2RhSn, and Fe_2RhGe, correspondingly. Our calculations suggest a possibility for the
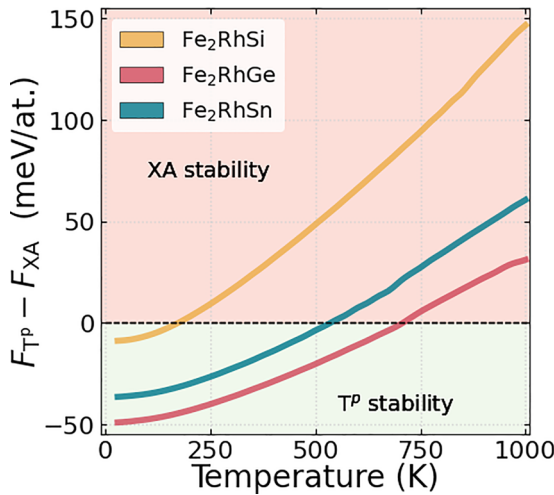
FIG. 2. Difference in free energy between the T^p and XA structures of Fe_2RhZ ($Z =$ Si, Ge, Sn). The additional information about all contributions to the free energy is given in the SM [36] (see Sec. II C).

synthesis of T^p structures in $Fe_2Rh(Si, Ge, Sn)$ under suitable annealing conditions.

C. Electronic structure

We now consider the electronic origins of the stability (instability) of the cubic phase and the band gap formation for Fe_2- and Rh_2-based Heusler families. The high-symmetry phase has been found to be unstable in many Heusler compounds with respect to the tetragonal distortion, especially the Mn-rich compounds. The different mechanisms are responsible for this, such as the Jahn-Teller effect [52], the nesting-induced Fermi surface instability [53,54], and anomalous phonon modes [55], which results in the peak-and-valley character of the DOS and the number of states near E_F in the cubic phase [45,56].

The total DOS profiles for the full set of Heusler alloys we have studied are presented in the SM [36] (see Sec. III, Figs. S5–S8). Our calculations have shown that HM properties are observed only in Fe_2RhSi of the XA-Fe_2RhZ series. The HM gap decreases and disappears with the replacement of Si by Ge and In, respectively. This is due to the weakening of covalent bonds and the enhancement of electron delocalization as the lattice parameter increases. Similar behavior is observed for Z from the third main group, except that the pseudogap is shifted towards the conducting band. For the T^p, T^c, and $T^\#$ structures, the degeneracy of the electron orbitals is removed and hence the DOS is smeared. For $L1_0$-Rh_2FeZ ($Z =$ Al, Ga, In) a HM pseudogap is observed in the valence band. For Z of the fourth main group, the pseudogap disappears, which is associated with a large tetragonal distortion.

In general, the correlation effects within the SCAN functional produce the basic features of the DOS already investigated earlier by the GGA-PBE for the set of Fe_2RhZ and Rh_2FeZ ($Z =$ Ga, In, Ge, Sn) [45]. However, the DOS curves produced by SCAN include an exchange splitting improvement with respect to PBE (see Fig. S5 in the SM [36]). This finding is due to the fact that the enhancement factor F_{xc} for the SCAN functional clearly depends on the iso-orbital indicator α based on the electron density, its gradients, and the kinetic energy density to describe covalent, metallic, and weak bonds [33]. In the case of GGA-PBE, α is equal to unity [57]. For SCAN, the strong variation of F_{xc} with respect to
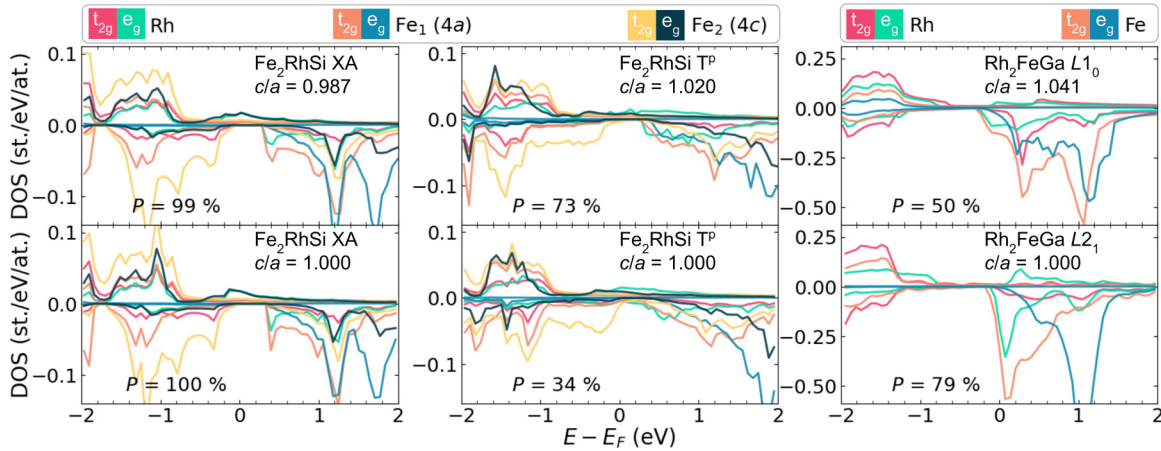
FIG. 3. The calculated orbital-resolved DOS for Fe_2RhSi and Rh_2FeGa in the cubic (XA and $L2_1$, $c/a = 1$) and slightly tetragonally distorted (XA, T^p, and $L1_0$, $c/a \approx 1$) structures. Here, Fe_1 and Fe_2 denote the Fe atoms located at nonequivalent positions (see Fig. S1 in the SM [36] for details). The DOS profiles for the cubic structures ($c/a = 1$) are calculated by fixing the cell volume of pseudocubic structures ($c/a \approx 1$). The total DOSs are shown in the SM [36] (see Sec. III, Figs. S6–S8).

α results in a negative value of the derivative $\delta F_{xc}/\delta\alpha$. As a consequence, an increase of magnetic moment leads to an increase and decrease of the spin-up and spin-down exchange enhancement factors, respectively, as well as to an increase of the exchange splitting [57].

Figure 3 presents the orbital-resolved DOSs for two representative compounds, Fe_2RhSi and Rh_2FeGa, as examples of the Fe_2- and Rh_2-based Heusler alloy families. In accordance with the full geometry optimization procedure, for both Fe_2RhSi and Rh_2FeGa, the cubic crystal structures XA and $L2_1$ as well as the considered T^p turn out to be slightly tetragonally distorted ($c/a \approx 1$). To illustrate the effect of the weak tetragonal distortion, we also presented the DOSs for Fe_2RhSi and Rh_2FeGa in the ideal cubic structures ($c/a = 1$) (see bottom panel of Fig. 3).

For the cases of Fe_2RhSi in the XA and T^p structures, DOS profiles of ideal and pseudocubic structures are almost similar in the entire energy range under study. The DOSs of the valence band arise from hybridization between the $Fe_{1(2)}$ and Rh orbitals with a predominant contribution from the Fe_2 atoms, while the DOSs of the conduction band are mainly contributed by the d electrons of the Fe_1 atoms. A slight distortion results in smoother DOSs in a pseudocubic phase than in the cubic one due to lowering the symmetry of crystals and their energy. As a consequence of this slight decrease in symmetry, the degeneration of overlapping bands along the taper direction of the crystal is eliminated and they become wider. This behavior is also known as the "fat band" effect. For instance, for the T^p structure, the merging of two peaks of Fe orbitals into one between -1.5 and -1.2 eV in the valence band as well as the shift of E_F are observed under distortion.

We see, generally, that for all four cases, the majority spin channel contributes weakly to the mechanism of slight tetragonal distortion because of the very low DOS values around E_F. The origin of the small tetragonal distortion of XA may be due to the elimination of degeneracy and, the broadening of the bands, which leads to the smearing of the DOS peaks [45,58]. Due to the broadening of bands, the width of the forbidden band decreases and the electrons

occupy new lower orbitals. Thus, with tetragonal distortion, the electronic contribution to the total energy decreases and the lattice contribution increases. However, the gain from the electronic contribution outweighs it. In the case of T^p there are two contributions leading to tetragonal distortion. The first is the aforementioned fat band effect. The second and likely the most important, the nonequivalent surroundings of the Fe and Rh atoms due to their layered ordering leads to chemical pressure and a shift of some electron states to lower energies relative to E_F.

Going from Fe_2RhSi to Rh_2FeGa, we see that the d electrons of Rh atoms contribute to a greater extent to the valence band than those of Fe atoms. As a result, the e_g orbitals of Rh participate only in hybridization with the t_{2g} orbitals in the spin-down channel.

Whereas the conduction band is attributed to the predominant contribution of Fe d orbitals, the minority spin channel has a high DOS (≈ 1 st/eV per atom) near E_F for the cubic $L2_1$ structure. The sense is preserved an electrostatic repulsion between the electrons becomes significant, resulting in an increase in energy and instability of the $L2_1$ phase. The Jahn-Teller distortion [11,47] reduces both the total energy and the DOS values of the lower symmetry $L1_0$ phase. As a consequence, the degeneracy of the orbitals is removed; the first DOS peak of the conductivity band observed at 0.29 eV for $c/a = 1$ shifts to 0.08 eV for $c/a \approx 1.04$; the DOS at E_F becomes smoothed.

It is also obvious from Fig. 3, both the XA and the T^p structures with $c/a = 1$ and $c/a \approx 1$ reveal the energy gap around E_F in the minority spin states, while the majority spin states are mainly arisen from the hybridization between the d orbitals of the Fe and Rh atoms. As a result, the HM behavior with the largest spin polarization ($P = 99\%$) is predicted for the XA-Fe_2RhSi ($c/a = 0.987$), respectively. However, the T^p-Fe_2RhSi and $L1_0$-Rh_2FeGa exhibit the smaller spin polarization, which is equal to 73% ($c/a = 1.02$) and 50% ($c/a = 1.041$), respectively. The P values as well as energy gap are sensitive to the volume of a cell, which can be directly changed through the application of an external pressure.
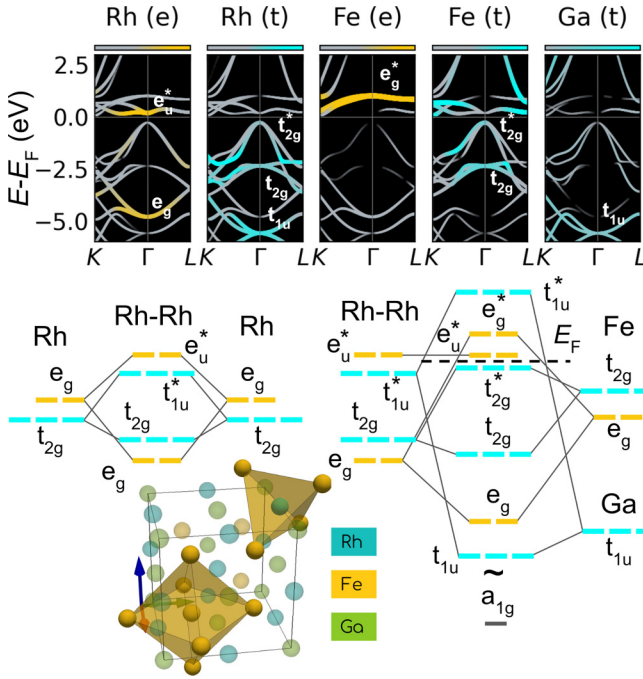
FIG. 4. Top panel: Band structure of the spin-down channel around the Γ point. Bottom panel: Hybridization scheme for the $L2_1$-Rh$_2$FeGa system. The nearest-neighbors symmetry illustrated in the cubic Heusler structure denotes the tetrahedral and octahedral environments for Fe and Rh, respectively.

To better understand the nature of pseudogap in Rh$_2$FeGa and a zero DOS with a band gap in Fe$_2$RhSi in the spin-down channel, we consider further the orbital splitting of the band structures near E_F, as shown in Figs. 4–6. In this case, we focus on Rh$_2$FeGa with the $L2_1$ ($c/a = 1$) and $L1_0$ ($c/a \approx 1.04$) structures and XA-Fe$_2$RhSi ($c/a = 1$), as an example.

We now consider the issues of the gap formation in the $L2_1$ structure of Rh$_2$FeGa (see Fig. 4). The formation of a HM gap in Heusler alloys was originally proposed by Galanakis *et al.* for $L2_1$-Co$_2$MnGe [27]. In general, the gap formation in the Heusler alloys with $4d$ transition metal elements is realized in a similar manner as for the $3d$ group Heusler alloys [27,59–62]. In the first step, the d orbitals of the Rh and Fe atoms split into two sets of orbitals in the octahedral and tetrahedral ligand fields, respectively, according to the crystal-field theory [63,64]. The e_g states of Rh have a higher energy, while the set of t_{2g} states has a lower energy. In the case of Fe, the order of the e_g and t_{2g} levels is reversed due to tetrahedral symmetry. The orbitals of the Rh atoms located at the equivalent sites $8c$, which have the O_h point symmetry (if we neglect the precipitating atoms), further hybridize with each other, producing two bonding orbitals (e_g and t_{2g}) and two antibonding orbitals (e_u^* and t_{1u}^*), which are unsymmetrical with respect to inversion (see the left scheme in Fig. 4).

These Rh-Rh d orbitals hybridize again with both the Fe $3d$ orbitals and the Ga $2p$ orbitals (see the right scheme in Fig. 4). As for hybridization between the Rh-Rh orbital complex (e_g, t_{2g}, t_{1u}^*, and e_u^*) and the Fe orbitals (e_g and t_{2g}),

it occurs similarly to the previous case, forming new e_g, t_{2g} bonding orbitals and e_g^*, t_{2g}^* antibonding orbitals. In this case, the e_u^* Rh-Rh orbital has no symmetry among the Fe and Ga orbitals and therefore remains unchanged only, whereas the t_{1u}^* Rh-Rh orbital hybridizes with the Ga t_{1u} orbital, forming the bonding and antibonding orbitals t_{1u} and t_{1u}^*, respectively. The t_{1u}^* orbital is shifted significantly above E_F and it is not shown on the band structure. Due to the very low energy level, the Ga s orbital, which corresponds to the a_{1g} orbital, is omitted from the band structure.

On the one hand, the given scheme differs from the scheme proposed by Galanakis *et al.* [27] for Co$_2$MnGe by the fact that the Fermi level passes between the antibonding e_u^* and t_{2g}^* orbitals. This difference is associated with the noninclusion of p orbitals to the hybridization scheme for Co$_2$MnGe [27]. But, on the other hand, this scheme is consistent with the Co$_2$MnSi hybridization scheme in the framework of the study of DFT and correlation effects [65]. However, in contrast to Co$_2$MnSi, the hybridized orbitals of Rh$_2$FeGa are created by merging the $4d$ electron orbitals, so their radius increases. Consequently, the Coulomb repulsion energy of the pair of electrons in one orbital decreases, which does not favor the formation of a high-spin complex responsible for the half-metallicity in a material.

As mentioned above, the instability of the $L2_1$ structure for Rh$_2$FeGa is driven by the Jahn-Teller distortion, therefore the hybridization scheme should be more complex, as shown in Fig. 5. Consequently, the point group of symmetry for the Rh environment decreases from O_h to D_{4h}. In this case, the Rh atom is surrounded by an elongated octahedron along the c axis, and the Rh d orbitals lined up along the distortion split smaller and separate from the other orbitals. The Fe atom has a tetrahedral environment in a similar way to the case of the $L2_1$-cubic structure. Nevertheless, the tetragonal distortion slightly changes the Fe tetrahedral environment, but not as much as the Rh octahedral environment. As a result, d orbitals of Fe atoms split more weakly than those of Rh atoms. In contrast to the $L2_1$ structure, the Rh and Fe atoms now have two degenerated e_g orbitals and three nondegenerated orbitals (a_{1g}, b_{1g}, and b_{2g}).

The first step of hybridization between Rh atoms occurs similarly to the $L2_1$ structure except that the level degeneracy of the d orbitals is lifted and hence the Rh-Rh orbital complex is formed from the five bonding orbitals (a_{1g}, b_{1g}, b_{2g}, and $2e_g$) and five antibonding orbitals (a_{1u}^*, b_{1u}^*, b_{2u}^*, and $2e_u^*$). In the second step, when the hybridization between the Rh-Rh complex and the Fe orbitals occurs, all antibonding Rh-Rh orbitals excepting e_u^*, remain unchanged due to the absence of similar symmetry orbitals. The e_u^* orbitals hybridize with the Ga p orbitals, shifting slightly from their original positions. The remaining bonding Rh-Rh orbitals and the Fe orbitals create corresponding bonding and antibonding hybrids, as illustrated in Fig. 5.

It is obvious that the energy of the a_{1g}^* antibonding orbital lies slightly below E_F in view of the Jahn-Teller distortion. Thus the ideal half-metallicity is destroyed, but the spin polarization at E_F is still high ($P = 50\%$). This finding suggests that the presence of the Jahn-Teller effect is not favorable for the emergence of half-metallicity, since it leads to a stronger splitting of the orbital energy levels and the disadvantage of
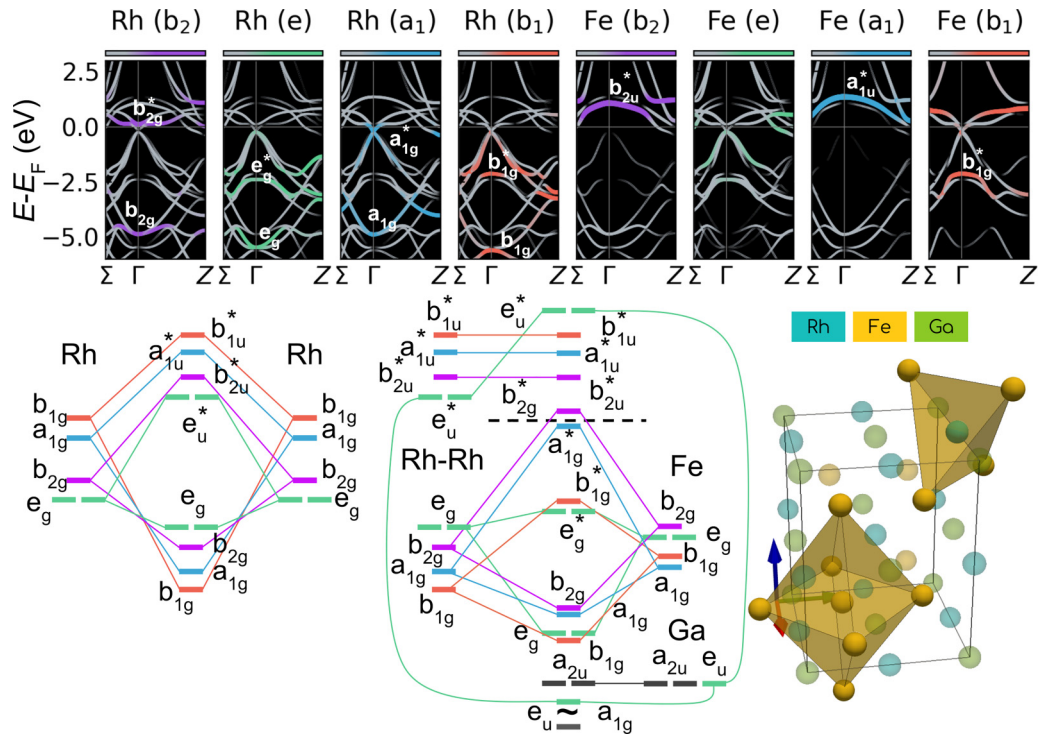
FIG. 5. Top panel: Band structure of the spin-down channel around the Γ point. Bottom panel: Hybridization scheme for the $L1_0$-Rh$_2$FeGa system ($c/a = 1.041$). The nearest-neighbors symmetry illustrated in the tetragonal Heusler structure denotes the tetrahedral and octahedral environments for Fe and Rh, respectively.
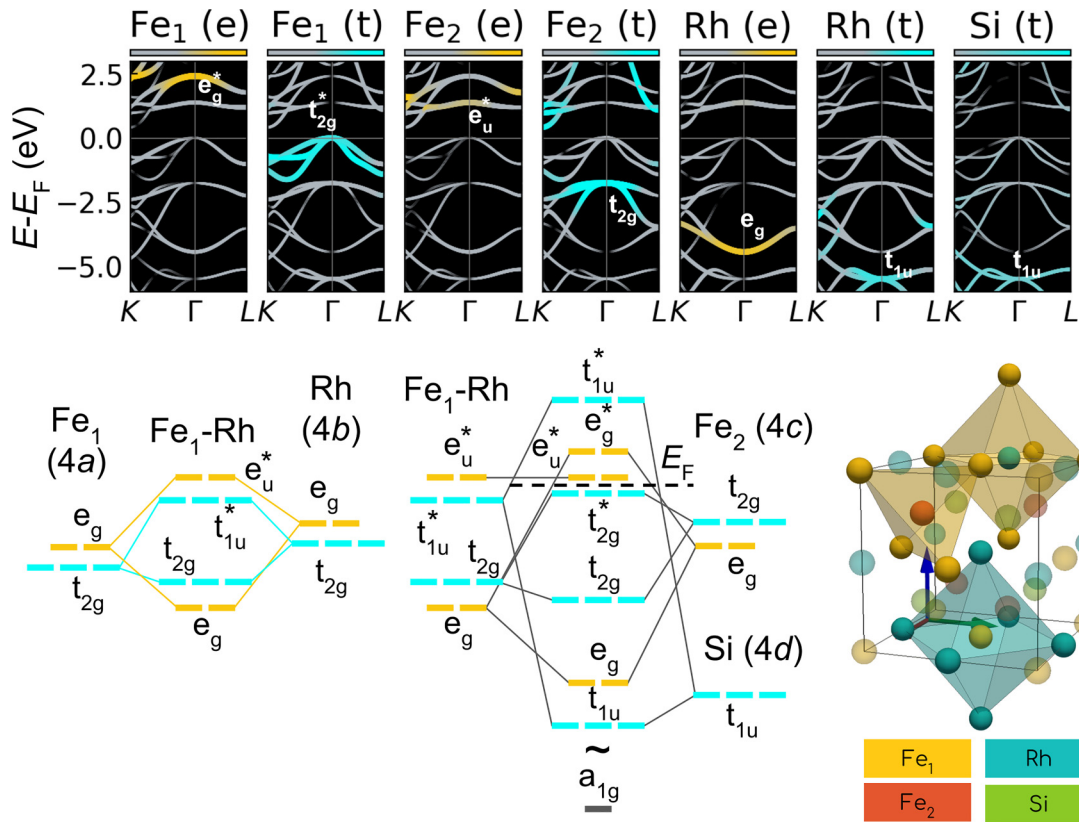
FIG. 6. Top panel: Band structure of the spin-down channel around the Γ point. Bottom panel: Hybridization scheme for the XA-Fe$_2$RhSi system ($c/a = 1.0$). The nearest-neighbors symmetry illustrated in the cubic Heusler structure denotes the tetrahedral and octahedral environments for Fe and Rh, respectively. Here $4a$, $4b$, $4c$, and $4d$ are the Wyckoff positions for the XA structure.
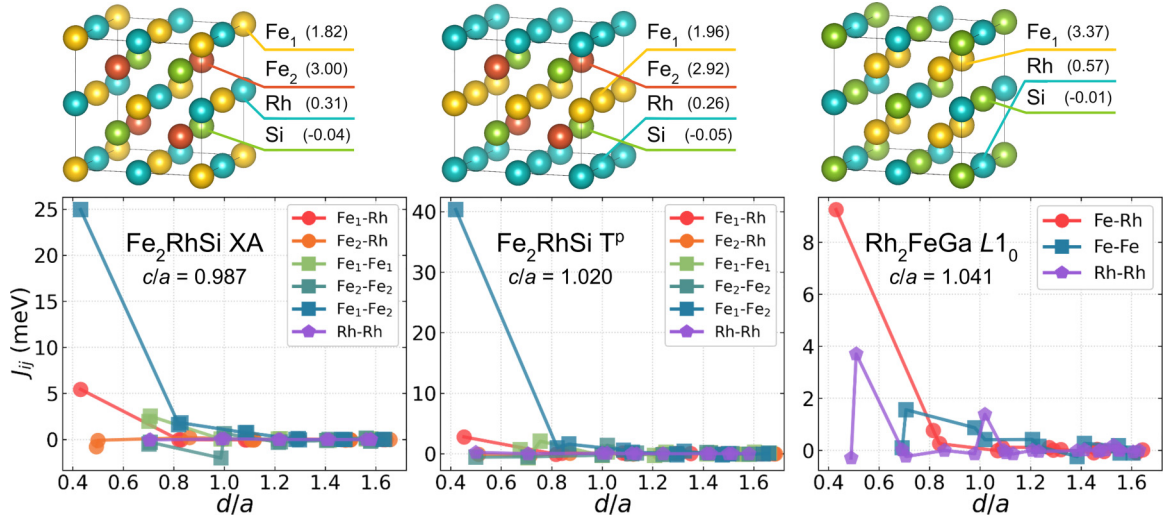
FIG. 7. The Heisenberg exchange parameters of XA- and T^p-Fe_2RhSi and $L1_0$-Rh_2FeGa as a function of distance d/a between the interacting pair of atoms. The interatomic distance is given in units of the respective lattice constant a. The interactions with Si and Ga atoms are not shown because they are negligibly small. Partial magnetic moments are presented in parentheses.

the high-spin complex. Nevertheless, the presence of a pseudogap between -0.3 and -1 eV in the minority spin channel of DOS for $L1_0$-Rh_2FeGa allows one to suppose that a nearly HM behavior can be obtained by a variation of cell volume or a slight deviation from the stoichiometry.

Let us consider the cubic XA-Fe_2RhSi compound that has the energy gap in the minority spin channel of DOS. The orbital hybridization mechanism of the HM gap is similar to that of the $L2_1$ structure (see Fig. 6). For the XA cubic structure, the Rh and Fe_1 atoms are in an octahedral environment, while the Fe_2 atoms are typified by a tetrahedral arrangement. According to crystal-field theory, during complex formation, the Rh and Fe_1 d orbitals split and form two sets of orbitals e_g and t_{2g}, where e_g levels lie higher in energy than t_{2g} levels. The splitting of the d orbitals of Fe_2 is opposite to the splitting of the d orbitals of Fe_1.

The Fe_1 orbitals are combined initially with the Rh orbitals located in the equivalent sites, creating the doublet e_g and e_u^* orbitals and the triplet t_{2g} and t_{2g}^* orbitals. The second step of hybridization is exactly the same as for the $L2_1$ lattice (see Fig. 4). The Fermi energy is found at the edge of the valence band created by the Fe_1-Rh hybridizing t_{2g}^* orbitals with the dominant contribution from Fe_1. We find that the antibonding t_{2g}^* and e_u^* orbitals, which are created by the Fe_1-Rh complex and Fe_2 atoms in the conduction and valence states, correspondingly, are responsible for the minority band gap at E_F. By analogy with Ref. [65], it is shown that the spin-down state of 12 valence electrons for XA-Fe_2RhSi occupies three Fe_1 t_{2g}^* orbitals, three Fe_2 t_{2g} orbitals, two Rh e_g orbitals, three Rh-Si hybridizing t_{1u} orbitals, and one Si a_{1g} orbital. The well-known SP rule is satisfied by our diagram for the Heusler alloys with the inverse XA structure. Our calculations within the SCAN functional predict well the integer value of $\mu_{tot} = 5.00\mu_B$ in accordance with the SP rule, $\mu_{tot} = N_{ve} - 24$. This finding indicates that the five electrons, forming μ_{tot}, occupy two e_u^* orbitals, two e_g^* orbitals, and one t_{1u}^* orbital in the spin-up state of the conduction band.

D. Magnetic exchange interactions and Curie temperatures

To apply materials in spintronics or thermoelectronics, they must retain magnetic order at finite temperatures and have a high Curie temperature, T_C. To calculate the T_C values within MC simulations, the Heisenberg exchange interaction parameters J_{ij} were firstly calculated. In Fig. 7, we present the interatomic magnetic exchange interactions for XA- and T^p-Fe_2RhSi and $L1_0$-Rh_2FeGa as an example. The results for other compounds under study are not qualitatively different from those presented in Fig. 7 and given in the SM [36] (see Sec. IV, Figs. S9 and S10).

For Fe_2RhSi, the ground state T^p structure is dominated by the Fe_1-Fe_2 nearest-neighbor FM interaction, which is twice larger than that of the XA structure. This finding is associated with a smaller distance between pairs of atoms in the T^p structure ($d/a \approx 0.414$), the stronger hybridization between the d orbitals of Fe atoms, and the larger partial magnetic moments of Fe_1 and Fe_2 in comparison with the XA structure ($d/a \approx 0.431$). However, for the subsequent coordination spheres, the Fe-Fe interactions of both T^p and XA are found to be sufficiently smaller but practically equal in magnitude. In addition, these interactions demonstrate a damped oscillatory character indicating the competition between FM and AFM couplings with increasing distance. The second-strongest interactions are the intrasublattice Fe-Rh interactions for both XA and T^p, which are significant only for the nearest neighbors. The Rh-Rh exchange interactions between the Rh atoms are negligible in the entire distance range under study.

In the case of $L1_0$-Rh_2FeGa, the largest interaction is observed between the nearest Fe-Rh pair of atoms due to the smallest distance ($d/a \approx 0.430$). An increase in the distance leads to vanishing of the Fe-Rh interactions, similar to XA- and T^p-Fe_2RhSi. In regard to Fe-Fe interactions, we find also a damped oscillatory evolution in a manner as for XA- and T^p-Fe_2RhSi with increasing d/a. For the Rh-Rh interactions, we observe again the oscillating damped behavior with two
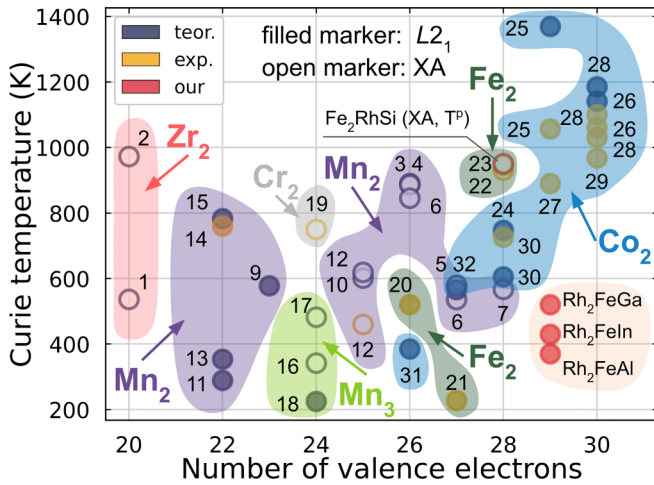
FIG. 8. The T_C values of HM or nearly HM Heusler alloys as a function of N_{ve}. The diagram displays our T_C values for Fe_2RhSi and $Rh_2Fe(Ga, In, Al)$ as well as for other compounds studied theoretically and experimentally:

1. Zr_2RhGa [66]	12. Mn_2RuGa [67,68]	23. Fe_2RhSi [29]
2. Zr_2RhIn [66]	13. Mn_2TiSn [69]	24. Co_2CrSi [70]
3. Mn_2CoAl [71]	14. Mn_2VAl [72]	25. Co_2FeGa [73,74]
4. Mn_2CoGa [71]	15. Mn_2VGa [75]	26. Co_2FeGe [73,74]
5. Mn_2CoGe [71]	16. Mn_3Al [76]	27. Co_2FeIn [74]
6. Mn_2CoIn [71]	17. Mn_3Ga [76]	28. Co_2FeSi [74,77,78]
7. Mn_2CoSb [71]	18. Mn_3Ga [67]	29. Co_2FeSn [74]
8. Mn_2CoSi [70]	19. Cr_2CoAl [79]	30. Co_2MnAl [77,80]
9. Mn_2CrGa [67]	20. Fe_2CrSi [81]	31. Co_2TiSi [70]
10. Mn_2FeGa [67]	21. Fe_2MnSi [81]	32. Co_2VSi [70]
11. Mn_2NbGa [67]	22. Fe_2RhGe [29]	

pronounced peaks and higher J_{ij} values than those of XA- and T^p-Fe_2RhSi.

The full set of J_{ij} constants allowed us to obtain temperature dependencies of magnetization using MC simulations of the Heisenberg model. The calculated Curie temperatures as well as thermomagnetization curves for the rest of the compounds (we study in this work) are presented in the SM (see Figs. S9–S11). In the case of light elements (Al, Si), the magnetization curves of the XA and T^p structures practically coincide. On going to heavier Z atoms, the magnetization curves diverge to a greater extent. This is due to an increase in the c/a ratio of crystal structures (see Table I). For $L1_0$-Rh_2FeZ, the magnetization and T_C values are slightly higher for Z = Al, Ga, and In as compared to Si, Ge, and Sn.

Figure 8 illustrates the T_C dependency with respect to the number of valence electrons N_{ve} for Fe_2RhSi and $Rh_2Fe(Ga, In, Al)$ in their ground state structures as well as for the known HM Heusler alloys investigated theoretically and experimentally in the previous studies [29,66–81]. We would like to emphasize that in accordance with the SP rule the three cases of half-metallicity are possible [11–13]: (i) for $N_{ve} < 24$, there is the band gap at E_F in the spin-up channel; (ii) for $N_{ve} = 24$, there is the spin-gapless character (a semimetallic feature for one channel and a semiconductor feature for the other spin channel); (iii) for $N_{ve} > 24$, there is the band gap at E_F in the spin-down channel.

For a visual approximation of the T_C values, it is convenient to highlight the main families of alloys on the diagram. Most of the presented compounds are the Mn- and Co-based Heusler families. The Mn-based alloys form three groups of HM or nearly HM compounds ($N_{ve} < 24$, $N_{ve} = 24$, and $N_{ve} > 24$) with the average T_C values ranging between 400 and 900 K. The majority of Co-based alloys with $N_{ve} > 24$ exhibit the largest T_C varied between 950 and 1200 K. As for Fe-based samples, $Fe_2(Cr,Mn)Si$ have smaller T_C values, $\approx$ 520 and 220 K, respectively. In contrast to $3d$ Fe-based compounds, $4d$ Fe_2RhSi systems predict high calculated Curie temperatures, $\approx$ 950 K for the XA structure ($P = 99\%$) and $\approx$ 1000 K for the ground state T^p structure ($P = 75\%$). Notice that our T_C values agree well with the experimental one, 940 K, for Fe_2RhSi [29]. This value is the highest among HM Heusler alloys with an XA lattice, as well as those containing $4d$ elements. Finally, Rh-based alloys are expected with a smaller T_C varied between $\approx$ 380 and 550 K due to weak exchange interactions, as shown in Fig. 7.

E. Transport properties

The efficiency of thermoelectric properties is determined by several parameters, including the Seebeck coefficient S, electrical and thermal conductivities, as well as the dimensionless parameter, figure of merit $ZT = S^2\sigma T/\kappa$, which is dependent on these quantities. Here σ is the electrical conductivity and κ is the thermal conductivity, consisting of the lattice (κ_L) and electronic (κ_e) parts. The overall efficacy of the material in thermoelectric applications is dependent on ZT. Two factors can maximize ZT: an increase in the value of power factor ($S^2\sigma$) and a decrease in the value of κ_L.

In general, the calculations of transport properties for XA-, T^p-Fe_2RhZ and $L1_0$-Rh_2FeZ revealed the following features. In all cases, the conductivity for spin-down electrons is found to be less than that of spin-up electrons (see the SM [36], Figs. S12 and S13). This finding is due to the lower DOS for the spin-down channel. Thermal conductivity increases linear with temperature for the electronic subsystem, and hyperbolic decreases for the lattice subsystem (see the SM [36], Figs. S14–S16). The Seebeck coefficient for XA- and T^p-Fe_2RhZ takes on large values only for Z = Si. In other cases, it is small, which is due to a metallic behavior and, consequently, a large electronic conductivity. For $L1_0$-Rh_2FeZ with Z = Al, Ga, and In the Seebeck coefficient is also large due to the presence of a HM pseudogap for the spin-down electrons (see the SM [36], Figs. S17–S19).

In Fig. 9 we present the temperature-dependent Seebeck coefficient and figure of merit ZT for both spin configurations of XA- and T^p-Fe_2RhSi and $L1_0$-Rh_2FeGa. The variations of electrical and thermal conductivities and Seebeck coefficients with a temperature are shown in the SM [36] (see Figs. S12–S19). We find that the spin-down channel contributes in the transport properties.

It is evident from the figures for Fe_2RhSi that the values of S in the entire temperature range are positive in the spin-down channel, signifying the presence of holes as majority carriers (p-type charge carriers). For the XA structure, as the temperature increases, the S coefficient increases from 180 μeV/K
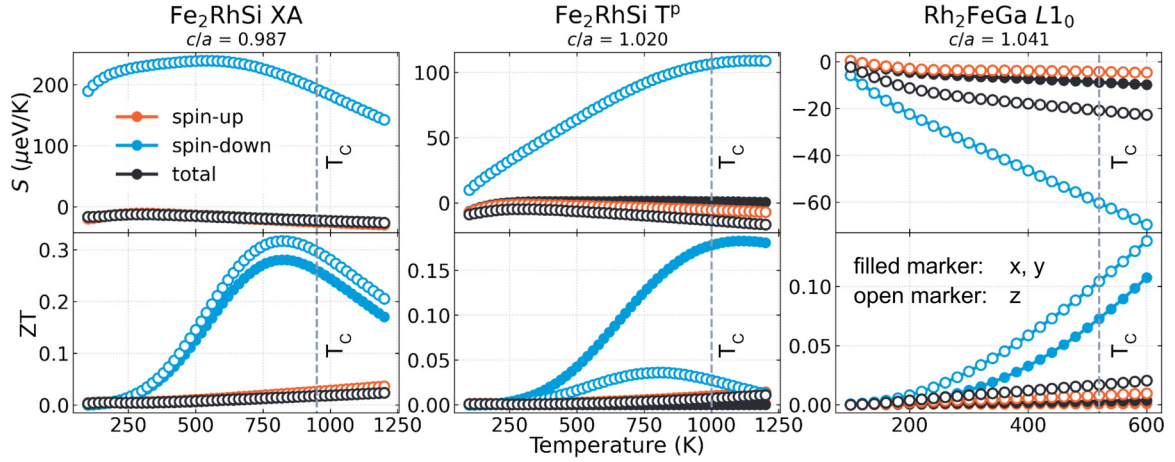
FIG. 9. The spin-resolved Seebeck coefficient (S) and figure of merit $ZT = S^2 \sigma T / \kappa$ of the XA- and T^p-Fe$_2$RhSi and $L1_0$-Rh$_2$FeGa as a function of temperature. The transport coefficients are presented along the $x = y$ (filled circle) and z (open circle) directions.

at 100 K, reaches the maximum value of 250 μeV/K, and decreases further to 150 μeV/K at 1200 K in the minority spin channel. In the case of the T^p structure, the variation of S in the spin-down channel shows twice smaller values. In addition, the splitting between the S_x and S_z components is clearly seen due to both the tetragonal symmetry and different atomic ordering in the x and z directions. However, this splitting is not significant for the almost symmetrical XA structure.

The large S values of both XA and T^p are due to the clear gap and pseudogap at E_F in the spin-down channel (see Fig. 3), correspondingly, and therefore, small variations of electrical conductivity with temperature are expected. The metallic spin-up channel of both XA and T^p is characterized by small and negative values of S due to the high conductivity of electrons as the main n-type charge carriers. It can also be seen that the inflection of the $S(T)$ curves at high temperatures falls at T_C.

In the case of Rh$_2$FeGa, the values of S in the entire temperature range are found to be negative in both spin channels, indicating the presence of electrons as majority n-type charge carriers. It is clear from the plots that S decreases with an increase in temperature. For the spin-down channel the slope of the $S(T)$ curve is sharper as compared to the spin-up channel. This behavior can be attributed to the presence of a pseudogap in the minority-spin valence band near E_F. The average change in S is comparable in absolute value to that of T^p-Fe$_2$RhSi. The slight anisotropy of the S coefficient in different directions can be also seen due to the small tetragonal distortion ($c/a = 1.041$). For instance, the Seebeck coefficient calculations for Zr$_2$RhZ show the smallest values in the spin-up metallic state and the largest values in the half-metallic spin-down state, 5.65 and -305.8 μeV/K for Z = Ga, and 7.7 and -753.4 μeV/K for Z = In [66].

Finally, we briefly comment on the variations of spin-resolved and total ZT factors with temperature (bottom panel of Fig. 9).

To calculate the ZT factor, $\kappa_L(T)$ dependencies were evaluated according Eq. (2) using the calculated values of the Debye temperature and Gruneisen parameter. The $\kappa_L(T)$ curves are presented in the SM [36] (see Fig. S16). We find that κ_L is calculated to be ≈ 22 and 15 W/(m$\times$s) for T^p- and

XA-Fe$_2$RhSi. The lower value of $\kappa_L(T)$ is related to the lower Debye temperature for XA-Fe$_2$RhSi. As mentioned above, the efficiency of energy conversion in thermoelectric materials is determined by the dimensionless figure of merit ZT, the value of which for known thermoelectric materials is given in Table III. The compounds that we have studied demonstrate sufficiently smaller values of ZT for the spin-down channel, which are about 0.025 and 0.01 for XA- and T^p-Fe$_2$RhSi, respectively, and 0.02 for $L1_0$-Rh$_2$FeGa at 300 K. As the temperature increases, ZT reaches an average value of $\approx$ 0.28 at 800 K for XA-Fe$_2$RhSi. For both T^p-Fe$_2$RhSi and $L1_0$-Rh$_2$FeGa, the value of ZT varies smaller with an increase in temperature in comparison with XA-Fe$_2$RhSi. In addition, there is the anisotropy of the ZT factor between the x and z directions, which is stronger for Fe$_2$RhSi with the T^p structure. We suggest that the studied compounds are of interest for further fundamental researches, in order to improve the transport properties by Fermi-level shifting and doping impurity atoms into the systems, dependent on extra electrons

TABLE III. Figure of merit ZT for semiconductor thermoelectric materials (top) and for full- and half-Heusler half-metal alloys (bottom). For half-metallic materials, the spin-up and spin-down channel values are given, respectively.

	300 K		800 K		Ref.
(Bi$_{0.25}$Sb$_0$.75)$_2$Te$_3$	1.41				[82]
Hf$_{0.75}$Zr$_{0.25}$NiSn	0.08		0.55		[83]
Hf$_{0.75}$Zr$_{0.25}$NiSn$_{0.975}$Sb$_{0.025}$	0.07		0.48		[84]
Co$_{0.2}$Fe$_{0.05}$Sb$_{0.75}$	0.03		0.49		[85]
PbTe	0.83				[84]
Zr$_2$RhGa[a]	0.00	0.84	0.02	0.79	[66]
Zr$_2$RhIn[a]	0.00	0.97	0.02	0.69	[66]
CrCaSn[a]	0.00	0.95	0.00	0.58	[86]
XA-Fe$_2$RhSi	0.03	0.23	0.03	0.21	
T^p-Fe$_2$RhSi	0.01	0.13	0.01	0.13	
$L1_0$-Rh$_2$FeGa	0.00	0.11	0.00	0.13	

[a]The calculations were performed with $\kappa_L = 0$ and the value of ZT is overestimated.

or holes, change the exchange potential between carriers, or replace atoms with heavier atoms to reduce κ_L.

IV. CONCLUSION

Fe- and Rh-based Heusler compounds Rh_2FeZ and Fe_2RhZ (Z = Al, Si, Ga, Ge, In, Sn) have been considered to study the effect of various atomic configurations and tetragonal distortion on their electronic, magnetic, half-metallic, and transport properties. For all Fe_2RhZ compounds except Fe_2RhIn, the T^p pseudocubic structure with layered ordering of Fe and Rh is predicted to be as the ground state, whereas the $T^{\#}$ structure is preferable for Fe_2RhIn. In the case of Rh_2Fe(Al, Ga, In), the ground state $L1_0$ structure with a slight tetragonal ratio ($c/a \gtrsim 1$) is predicted, while the Rh_2Fe(Si, Ge, Sn) compounds have the $L1_0$ structure with $c/a \approx 1.2$. Within the convex hull analysis we find that all considered compounds are stable or metastable against the decomposition into stable binary compounds. It is shown that for the most studied compounds, the presence of a $4d$ Rh atom makes the formation of a high-spin complex unfavorable due to a decrease in the Coulomb repulsion of electrons and a high electron density at the Fermi level, and, as a consequence, the appearance of the Jahn-Teller effect and the metallic character of the electronic structure.

Out of the 12 studied compounds, only Fe_2RhSi with the XA structure possesses 100% spin polarization and an integer magnetization of $5\mu_B$ due to a band gap for the minority spin channel at E_F. According to the band structure and hybridization scheme, we find that the Fermi level lies between the antibonding t_{2g}^* and e_u^* orbitals, which are created by the Fe_1-Rh complex and the Fe_2 atom. Due to the highest spin polarization, XA-Fe_2RhSi demonstrates large enough values of Seebeck coefficient and figure of merit for the spin-down channel. However, Fe_2RhSi in the ground state T^p structure with $5.02\mu_B$ possesses a smaller polarization (73%) due to a pseudogap for the minority spin channel at E_F. For both XA- and T^p-Fe_2RhSi, the calculated Curie temperatures are about 950 and 1000 K, respectively, which are consistent with the experimental observations ($T_C = 940$ K) [29]. We believe that the present results may be of interest for further fundamental and experimental researches and become a material platform for spintronics and spin-caloric applications.

[1] C. Tsirogiannis and I. Galanakis, J. Magn. Magn. Mater. **393**, 297 (2015).

[2] S. Ram, M. R. Chauhan, K. Agarwal, and V. Kanchana, Philos. Mag. Lett. **91**, 545 (2011).

[3] H. C. Kandpal, G. H. Fecher, C. Felser, and G. Schönhense, Phys. Rev. B **73**, 094422 (2006).

[4] S. Jana, K. Sharma, and P. Samal, J. Chem. Phys. **149**, 164703 (2018).

[5] Y. Zhang, D. A. Kitchaev, J. Yang, T. Chen, S. T. Dacek, R. A. Sarmiento-Pérez, M. A. L. Marques, H. Peng, G. Ceder, J. P. Perdew, and J. Sun, npj Comput. Mater. **4**, 9 (2018).

[6] E. B. Isaacs and C. Wolverton, Phys. Rev. Mater. **2**, 063801 (2018).

[7] Z.-H. Yang, H. Peng, J. Sun, and J. P. Perdew, Phys. Rev. B **93**, 205205 (2016).

[8] V. Sokolovskiy, D. Baigutlin, O. Miroshkina, and V. Buchelnikov, Metals **13**, 728 (2023).

[9] K. Elphick, W. Frost, M. Samiepour, T. Kubota, K. Takanashi, H. Sukegawa, S. Mitani, and A. Hirohata, Sci. Technol. Adv. Mater. **22**, 235 (2021).

[10] T. Graf, C. Felser, and S. S. Parkin, Prog. Solid State Chem. **39**, 1 (2011).

[11] C. Felser, L. Wollmann, S. Chadov, G. H. Fecher, and S. S. Parkin, APL Mater. **3**, 041518 (2015).

[12] V. Marchenkov and V. Y. Irkhin, Phys. Met. Metallogr. **122**, 1133 (2021).

[13] V. Marchenkov, V. Y. Irkhin, and A. Semiannikova, J. Supercond. Nov. Magn. **35**, 2153 (2022).

[14] Y. Nishino, S. Deguchi, and U. Mizutani, Phys. Rev. B **74**, 115115 (2006).

[15] D. Amari, M. Mokhtari, F. Dahmane, T. Belfarh, A. Tabeti, M. Elkeurti, and R. Khenata, Chin. J. Phys. **60**, 450 (2019).

[16] Z.-Y. Deng and J.-M. Zhang, J. Magn. Magn. Mater. **397**, 120 (2016).

[17] M. K. Hussain, O. T. Hassan, and A. M. Algubili, J. Electron. Mater. **47**, 6221 (2018).

[18] H. Li, Y.-C. Gao, X. Wang, and L.-Y. Wang, J. Supercond. Nov. Magn. **29**, 493 (2016).

[19] A. Birsan and V. Kuncser, J. Alloys Compd. **900**, 163491 (2022).

[20] X.-H. Kang and J.-M. Zhang, Solid State Commun. **264**, 19 (2017).

[21] A. Candan, J. Electron. Mater. **48**, 7608 (2019).

[22] A. Iftikhar, A. Ahmad, I. Ahmad, and M. Rizwan, Int. J. Mod. Phys. B **32**, 1850045 (2018).

[23] S. Mondal, C. Mazumdar, R. Ranganathan, E. Alleno, P. C. Sreeparvathy, V. Kanchana, and G. Vaitheeswaran, Phys. Rev. B **98**, 205130 (2018).

[24] M. Rizwan, A. Afaq, and A. Aneeza, Phys. B: Condens. Matter **537**, 225 (2018).

[25] M. El Amine Monir, H. Ullah, H. Baltach, and Y. Mouchaal, J. Supercond. Nov. Magn. **31**, 2233 (2018).

[26] F. Khelfaoui, A. Boudali, A. Bentayeb, L. El Hachemi Omari, and Y. Si Abderrahmane, Acta Phys. Pol., A **133**, 157 (2018).

[27] I. Galanakis, P. H. Dederichs, and N. Papanikolaou, Phys. Rev. B **66**, 174429 (2002).

[28] S. Ghosh and S. Ghosh, Phys. Scr. **94**, 125001 (2019).

[29] Y. Venkateswara, S. S. Samatham, A. K. Patel, P. D. Babu, M. R. Varma, K. G. Suresh, and A. Alam, Phys. Rev. B **104**, 094402 (2021).

[30] P. Neibecker, M. E. Gruner, X. Xu, R. Kainuma, W. Petry, R. Pentcheva, and M. Leitner, Phys. Rev. B **96**, 165131 (2017).

[31] V. V. Sokolovskiy, O. N. Miroshkina, V. D. Buchelnikov, and M. E. Gruner, Phys. Rev. Mater. **6**, 025402 (2022).

[32] G. Kresse and D. Joubert, Phys. Rev. B **59**, 1758 (1999).

[33] J. Sun, A. Ruzsinszky, and J. P. Perdew, Phys. Rev. Lett. **115**, 036402 (2015).

[34] (i) The alloys under study contain strongly correlated $3d$ and $4d$ transition metals. (ii) It is known that exchange-correlation functionals, which depend on electron density such as LDA and GGA, underestimate the width of the energy gap in semiconductors and half-metals [7,87,88], or even fail to predict the gap [8,89]. Therefore, there is a discontinuity in the derivative of the exchange-correlation functional with respect to electron density [90], which is exactly zero [90–92]. This leads to accounting for false self-interaction in the occupied states, which redistributes them and increases their energy, thereby reducing the gap.

[35] Additionally, all nonequivalent antiferromagnetic (AFM) configurations generated by permutations in the 16-atom cell were considered. Accordingly, for $L1_0$-Rh$_2$FeZ, two AFM configurations were considered; for XA-Rh$_2$FeZ and XA-, T^p-Fe$_2$RhZ, four configurations were considered; for T^c- and T$^\#$-Fe$_2$RhZ, five configurations were considered. All AFM configurations were found to be unfavorable. The average energy difference between AFM and FM states is $\approx$150–250 meV/atom. See the SM [36], Tables SII and SIII.

[36] See Supplemental Material at http://link.aps.org/supplemental/10.1103/PhysRevB.107.245130 for additional computation details and a brief description of the electronic structure and the magnetic and transport properties. The Supplemental Material also contains Refs. [93–95] devoted to the calculation of mechanical properties, Ref. [96] describing the quasiharmonic Debye model, Ref. [97] on the AFLOW database, and Refs. [98,99] containing data on the transport properties of the Heusler alloys.

[37] A. I. Liechtenstein, M. Katsnelson, V. Antropov, and V. Gubanov, J. Magn. Magn. Mater. **67**, 65 (1987).

[38] X. He, N. Helbig, M. J. Verstraete, and E. Bousquet, Comput. Phys. Commun. **264**, 107938 (2021).

[39] G. H. Wannier, Phys. Rev. **52**, 191 (1937).

[40] G. Pizzi, V. Vitale, R. Arita, S. Blügel, F. Freimuth, G. Géranton, M. Gibertini, D. Gresch, C. Johnson, T. Koretsune *et al.*, J. Phys.: Condens. Matter **32**, 165902 (2020).

[41] P. Asselin, R. F. L. Evans, J. Barker, R. W. Chantrell, R. Yanes, O. Chubykalo-Fesenko, D. Hinzke, and U. Nowak, Phys. Rev. B **82**, 054415 (2010).

[42] G. Pizzi, D. Volja, B. Kozinsky, M. Fornari, and N. Marzari, Comput. Phys. Commun. **185**, 422 (2014).

[43] S. A. Sofi and D. C. Gupta, Int. J. Energy Res. **45**, 4652 (2021).

[44] M. Yin and P. Nash, J. Alloys Compd. **650**, 925 (2015).

[45] S. V. Faleev, Y. Ferrante, J. Jeong, M. G. Samant, B. Jones, and S. S. P. Parkin, Phys. Rev. Appl. **7**, 034022 (2017).

[46] O. Osafile and J. Umukoro, Scientia Africana **19**, 167 (2021).

[47] P. Brown, A. Y. Bargawi, J. Crangle, K.-U. Neumann, and K. Ziebeck, J. Phys.: Condens. Matter **11**, 4715 (1999).

[48] A. Jain, S. P. Ong, G. Hautier, W. Chen, W. D. Richards, S. Dacek, S. Cholia, D. Gunter, D. Skinner, G. Ceder *et al.*, APL Mater. **1**, 011002 (2013).

[49] I. Frantsevich, F. Voronov, and S. Bakuta, *Handbook on Elastic Constants and Moduli of Elasticity for Metals and Nonmetals* (Naukova Dumka, Kiev, 1982), p. 288.

[50] S. I. Ranganathan and M. Ostoja-Starzewski, Phys. Rev. Lett. **101**, 055504 (2008).

[51] V. V. Sokolovskiy, M. E. Gruner, P. Entel, M. Acet, A. Çakır, D. R. Baigutlin, and V. D. Buchelnikov, Phys. Rev. Mater. **3**, 084413 (2019).

[52] C. Felser, G. H. Fecher, and B. Balke, Angew. Chem. Int. Ed. **46**, 668 (2007).

[53] A. T. Zayak, P. Entel, K. M. Rabe, W. A. Adeagbo, and M. Acet, Phys. Rev. B **72**, 054113 (2005).

[54] D. R. Baigutlin, V. V. Sokolovskiy, O. N. Miroshkina, M. A. Zagrebin, J. Nokelainen, A. Pulkkinen, B. Barbiellini, K. Pussi, E. Lähderanta, V. D. Buchelnikov, and A. T. Zayak, Phys. Rev. B **102**, 045127 (2020).

[55] A. Zheludev, S. M. Shapiro, P. Wochner, A. Schwartz, M. Wall, and L. E. Tanner, Phys. Rev. B **51**, 11310 (1995).

[56] Y. Matsushita, G. Madjarova, J. Dewhurst, S. Shallcross, C. Felser, S. Sharma, and E. Gross, J. Phys. D: Appl. Phys. **50**, 095002 (2017).

[57] F. Tran, G. Baudesson, J. Carrete, G. K. H. Madsen, P. Blaha, K. Schwarz, and D. J. Singh, Phys. Rev. B **102**, 024407 (2020).

[58] J. Suits, Solid State Commun. **18**, 423 (1976).

[59] S. Galehgirian and F. Ahmadian, Solid State Commun. **202**, 52 (2015).

[60] H. Luo, Z. Zhu, G. Liu, S. Xu, G. Wu, H. Liu, J. Qu, and Y. Li, J. Magn. Magn. Mater. **320**, 421 (2008).

[61] F. Ahmadian, J. Alloys Compd. **576**, 279 (2013).

[62] P.-L. Yan, J.-M. Zhang, and K.-W. Xu, J. Magn. Magn. Mater. **391**, 43 (2015).

[63] H. Bethe, Ann. Phys. **395**, 133 (1929).

[64] J. Van Vleck, Phys. Rev. **41**, 208 (1932).

[65] K. Nawa and Y. Miura, RSC Adv. **9**, 30462 (2019).

[66] M. J. Alrahamneh, J. M. Khalifeh, and A. A. Mousa, Phys. B: Condens. Matter **581**, 411941 (2020).

[67] L. Wollmann, S. Chadov, J. Kübler, and C. Felser, Phys. Rev. B **90**, 214420 (2014).

[68] T. Hori, M. Akimitsu, H. Miki, K. Ohoyoama, and Y. Yamaguchi, Appl. Phys. A **74**, s737 (2002).

[69] M. Meinert, J.-M. Schmalhorst, and G. Reiss, J. Phys.: Condens. Matter **23**, 036001 (2011).

[70] X.-Q. Chen, R. Podloucky, and P. Rogl, J. Appl. Phys. **100**, 113901 (2006).

[71] M. Meinert, J.-M. Schmalhorst, and G. Reiss, J. Phys.: Condens. Matter **23**, 116005 (2011).

[72] Y. Yoshida, M. Kawakami, and T. Nakamichi, J. Phys. Soc. Jpn. **50**, 2203 (1981).

[73] B. Balke, S. Wurmehl, G. H. Fecher, C. Felser, and J. Kübler, Sci. Technol. Adv. Mater. **9**, 014102 (2008).

[74] N. Kourov, V. Marchenkov, Y. A. Perevozchikova, and H. Weber, Phys. Solid State **59**, 898 (2017).

[75] K. R. Kumar, N. H. Kumar, G. Markandeyulu, J. A. Chelvane, V. Neu, and P. Babu, J. Magn. Magn. Mater. **320**, 2737 (2008).

[76] J. Kübler, J. Phys.: Condens. Matter **18**, 9795 (2006).

[77] J. Kübler, G. H. Fecher, and C. Felser, Phys. Rev. B **76**, 024414 (2007).

[78] S. Wurmehl, G. H. Fecher, H. C. Kandpal, V. Ksenofontov, C. Felser, H.-J. Lin, and J. Morais, Phys. Rev. B **72**, 184434 (2005).

[79] M. E. Jamer, L. G. Marshall, G. E. Sterbinsky, L. H. Lewis, and D. Heiman, J. Magn. Magn. Mater. **394**, 32 (2015).

[80] R. Umetsu, K. Kobayashi, A. Fujita, R. Kainuma, and K. Ishida, J. Appl. Phys. **103**, 07D718 (2008).

[81] H. Luo, Z. Zhu, L. Ma, S. Xu, H. Liu, J. Qu, Y. Li, and G. Wu, J. Phys. D: Appl. Phys. **40**, 7121 (2007).

[82] O. Yamashita, S. Tomiyoshi, and K. Makita, J. Appl. Phys. **93**, 368 (2003).

[83] T. Zhu, C. Fu, H. Xie, Y. Liu, and X. Zhao, Adv. Energy Mater. **5**, 1500588 (2015).

[84] J. R. Sootsman, D. Y. Chung, and M. G. Kanatzidis, Angew. Chem. Int. Ed. **48**, 8616 (2009).

[85] Y. Liu, X. Li, Q. Zhang, C. Chen, J. Li, L. Zhang, D. Yu, Y. Tian, and B. Xu, J. Mater. Sci.: Mater. Electron. **27**, 6433 (2016).

[86] D.-K. Shin and I.-H. Kim, J. Electron. Mater. **45**, 1234 (2016).

[87] K. Pokharel, J. W. Furness, Y. Yao, V. Blum, T. J. Irons, A. M. Teale, and J. Sun, J. Chem. Phys. **157**, 174106 (2022).

[88] B. Patra, S. Jana, L. A. Constantin, and P. Samal, Phys. Rev. B **100**, 045147 (2019).

[89] H. Xiao, J. Tahir-Kheli, and W. A. Goddard III, J. Phys. Chem. Lett. **2**, 212 (2011).

[90] L. J. Sham and M. Schlüter, Phys. Rev. Lett. **51**, 1888 (1983).

[91] R. W. Godby, M. Schlüter, and L. J. Sham, Phys. Rev. Lett. **56**, 2415 (1986).

[92] L. J. Sham and M. Schlüter, Phys. Rev. B **32**, 3883 (1985).

[93] R. Hill, Proc. R. Soc. London Ser. A **65**, 349 (1952).

[94] C. Zener, Phys. Rev. **82**, 403 (1951).

[95] A. Reuß, Z. Angew. Math. Mech. **9**, 49 (1929).

[96] M. Blanco, E. Francisco, and V. Luana, Comput. Phys. Commun. **158**, 57 (2004).

[97] M. Esters, C. Oses, S. Divilov, H. Eckert, R. Friedrich, D. Hicks, M. J. Mehl, F. Rose, A. Smolyanyuk, A. Calzolari *et al.*, Comput. Mater. Sci. **216**, 111808 (2023).

[98] Y. El Krimi and R. Masrour, Mater. Sci. Eng. B **284**, 115906 (2022).

[99] S. Sharma and S. K. Pandey, Phys. Lett. A **379**, 2357 (2015).